Characterization of internal tide non-stationarity : Eulerian versus Lagrangian perspectives

Zoé Caspar-Cohen*, Aurélien Ponte

Ifremer,Université de Brest, CNRS,IRD, Laboratoire d'Océanographie Physique et Spatiale (LOPS), IUEM,Brest,France

Noé Lahaye

Inria, IRMAR, campus universitaire de Beaulieu, Rennes, France

Xavier Carton, Xiaolong Yu and Sylvie Le Gentil

Ifremer,Université de Brest, CNRS,IRD, Laboratoire d'Océanographie Physique et Spatiale (LOPS), IUEM,Brest,France

Corresponding author: Zoé Caspar-Cohen, zoe.caspar@ifremer.fr

ABSTRACT

The Lagrangian and Eulerian near-surface current signatures of a low-mode internal tide propagating through a turbulent jet are compared in an idealized numerical simulation. We estimate and compare internal tides' stationary and nonstationary velocity amplitudes as well as non-stationarity timescales. We find Lagrangian internal tides total amplitude similar to Eulerian one. Lagrangian velocity are mostly nonstationary and Lagrangian non-stationary timescales are comparable to or smaller than Eulerian ones. This low-bias is proposed to be the result of the deformation of internal tide surface signal along the drift induced by lower frequency surface currents. A model based on the latter hypothesis successfully predicts Lagrangian autocovariance and highlights its dependence to Eulerian autocovariance and to the properties of the internal tides and jet. We address the implications of these results in the context of the Surface Water and Ocean Topography (SWOT) mission, for which the separation of mesoscale balanced flow and internal tides with data at the ocean's surface was raised.

1. Introduction

The disentangling of internal tides and balanced flow is a key issue for the Surface Water and Ocean Topography (SWOT) mission (Morrow et al. 2019). This wide-swath altimeter mission will provide instantaneous 2D sea level maps, with an expected horizontal resolution of the order of 15–30 km (Morrow et al. 2019; Fu et al. 2012). With this resolution, internal tides and mesoscale balanced flow will be captured, providing a unique opportunity to study both motions and their interaction. While both motions have distinct time scales, they can have similar length scales (order of hundreds of kilometers) which makes their separation by spatial filtering difficult. SWOT coarse temporal resolution (20 day repeat time approximately) will also prevent a separation by temporal filtering. Due to these two issues, internal tides and balanced flow will be entangled in SWOT data, which is problematic for estimates of surface currents via geostrophy.

Internal tides (or baroclinic tides) are internal waves generated by the barotropic tide when it passes over a topography (Garrett and Kunze 2007). Internal tides that are phase-locked with the tidal forcing are referred to as stationary internal tides. Stationary internal tides are predictable as they are phase-locked and of known amplitude. A fraction of the internal tides energy (mainly high modes) dissipates close to their generation's location (Whalen et al. 2020) but a significant part travels in the open ocean over potentially great distances – up to thousands of kilometers – with a low-mode vertical structure. As they travel, internal tides encounter variations of the background stratification as well as obstacles (continental shelf, islands, etc) which can cause energy dissipation or scattering toward higher modes (Whalen et al. 2020; Savva and Vanneste 2018; Savage et al. 2020). Internal tides can also become nonstationary. In particular, loss of stationarity has been observed when internal tides travel in a background stratification that varies in time (Buijsman et al. 2017), or pass through a turbulent jet (Ponte and Klein 2015; Dunphy

et al. 2017; Savage et al. 2020). They also become nonstationary when they reach the continental shelf (Nash et al. 2012b,a).

Several works used altimeter observations to study baroclinic tide including its non-stationary component (Ray and Zaron 2016; Zaron 2017, 2019; Nelson et al. 2019). To overcome limitations of altimeter data, the use of the global drifter program (GDP) dataset has been investigated in addition to the altimeter data (Zaron 2017, 2019; Nelson et al. 2019). The GDP complete dataset, combining Argos and GPS localisation system, is available interpolated over a temporal grid of 1h (Elipot et al. 2016). Lately, the number of drifters localised via GPS has increased, with only GPS tracked drifters recently deployed, thus decreasing the localisation error in the data (Elipot et al. 2016). This dataset has already been used to investigate high frequency near-surface near-inertial oscillations (NIOs) (Elipot et al. 2010).

There are however challenges and questions raised by the use of Lagrangian data. One of the challenges associated with the analysis and interpretation of Lagrangian data is that data collected by a drifter as it moves along with the flow may entangle Eulerian spatial and temporal variability and, give a deformed perspective of the Eulerian field. (LaCasce 2008) reviewed conceptual frameworks that have been developed in order to tackle this issue (Lumpkin et al. 2002; Middleton 1985; Davis 1983, 1985). Two regimes are typically identified : fixed float and frozen turbulence. The prevalence of one regime over the other is determined by the parameter $\alpha = T_E/T_a$, where T_E is the Eulerian evolution timescale of the flow and T_a is the time required for a drifter to travel the Eulerian characteristic spatial scale of the observed fluctuation. T_a is given by L/U, with U corresponding to an advection velocity and L the fluctuation's spatial scale. If $\alpha \ll 1$, the time required for the drifter to travel the length L is greater than the timescale of the fluctuation, T_E. In this case, one can expect an agreement between the Lagrangian and Eulerian timescales. Conversely, if $\alpha \gg 1$, it takes a drifter a time smaller than T_E to travel a distance L, causing

a more rapid fluctuation in the Lagrangian perspective. In this paper we apply these ideas to fit the case of internal tides interacting with a turbulent jet.

(Zaron and Elipot 2020) found a spectral broadening of the barotropic tide peaks in Lagrangian data compared to the Eulerian one, due to flow and/or tides spatial non-stationarity. It is therefore not trivial that Lagrangian drifter data may be used to study internal tides and their loss of stationarity depending on the regions of the ocean and the associated dynamical regime. It is also necessary to evaluate the use of Lagrangian data in the context of SWOT. Can Lagrangian data be used to filter and identify internal tides? In this study, we compare the non-stationarity timescales and amplitudes of an internal tide field crossing a turbulent jet, in Eulerian and Lagrangian frameworks. This allows us to test analytical models describing balanced flow and internal tides in an idealized set-up and the relationship of Eulerian and Lagrangian timescales.

We first present the numerical set-up used in this study as well as the method and model used to estimate signal amplitudes and decorrelation timescales. The results are shown in the second part for one simulation at first and several simulations varying the jet's strength later, . Lastly, we develop a theoretical model to predict Lagrangian autocovariance from Eulerian one and confront our results to it.

2. Numerical simulations and Lagrangian data

a. Numerical simulations

Idealized numerical simulations of an internal tide crossing a turbulent jet are considered. The numerical model is the Coastal and Regional Ocean COmunity model (CROCO) solving the hydrostatic equations. Its configuration follows Ponte et al. (2017) with a rectangular numerical domain (1024 km x 3072 km), zonally periodic. The Coriolis frequency follows the beta-plane approximation and is defined so that the domain is representative of mid-latitudes. A turbulent zonal jet crosses the domain at its center

along the meridional direction. It results from initialising the numerical simulation with a baroclinically unstable jet and is maintained by relaxing zonally averaged fields (velocities, temperature, sea level) toward the initial jet. Simulations with different turbulent jet strength are obtained by modulating the strength of the initial jet or equivalently the latitudinal thermal gradient. After 500 days, relaxation of the zonal mean fields toward the initial jet is ceased. The jet has a mean velocity amplitude maximum around 1450km in the center of the jet (Fig.1a, red line). The jet's amplitude decays over the observed period of time with a maximum around 0.6 m/s at the beginning and around 0.4 m/s at the end. The jet's velocity is computed by averaging each velocity component (u and v) over 2 days.

A mode-1 internal wave is generated at $y = 400$ km with a semi-diurnal frequency (2 cpd). Its signature at the surface contributes significantly to the total velocity amplitude in the northern and southern areas (Fig.1a, green line compared to red line). Sponge layers are put on the top and the bottom of the domain ($y < 300$ km and $y > 2700$ km). About 8000 simulated near surface drifters (referred to as drifters in the rest of this study) are also initialised at day 500 on a regular grid extending from 600 km to 2400 km and their advection is performed online (Fig.1b).

b. Lagrangian outputs overview

In the central part of the domain, the jet turbulence dominates the drifter net motion with a displacement of about 300 km in the x-direction and 160 km in the y-direction, i.e. an internal tide wavelength, over a 40 day time window (Fig.2c). When averaged over all drifters in this area, the net displacement over such time window is about 200 km. Away from the jet (Fig.2a and e), the net distance travelled by selected drifters, in the y-direction, is of about 20–30 km which is a fraction of an internal tide wavelength. Internal tides produce on the other hand periodical displacements of the order of 2–3 km. Eulerian

and Lagrangian zonal velocity time series exhibit significant differences in the jet at both low and internal tide frequency (modulation of the envelope and phase) over the 40 day temporal window (Fig2d). To quantify these differences, we will estimate amplitude and decorrelation/nonstationary time scales associated with the jet and internal tides and compare the results in different parts of the domain.

Zonal velocity time series outside the jet (Fig2b and f) exhibit weaker differences between both perspectives, as seen from their envelopes. Modulations of internal tide fluctuations in the south and north parts of the domain differ markedly from each other with faster fluctuations of their envelope in the north compared to the south. This feature occurs in both Eulerian and Lagrangian time series and reflects the loss of stationarity of the internal tide as it propagates northward and interacts with the turbulent jet.

c. Methods

1) Estimation of Eulerian and Lagrangian amplitudes and timescales

We estimate the amplitudes and decorrelation timescales of slow and fast motions by computing the velocity autocovariance in Eulerian and Lagrangian model outputs and fitting it to a theoretical model for a superposition of two motions (fast and slow) keeping timescales and amplitudes as variables. We assume a velocity component v may be written as the sum of an internal tide part $\widetilde{v}$ and a turbulent (or jet) part $\overline{v}$:

$$v = \widetilde{v} + \overline{v} \tag{1}$$

Assuming internal tide velocities and jet velocities are uncorrelated, the total autocovariance, C, equals to the sum of the autocovariances of $\widetilde{v}$ and $\overline{v}$:

$$C(\tau) = \langle v(t)v(t+\tau)\rangle = \widetilde{C}(\tau) + \overline{C}(\tau), \tag{2}$$

where $\langle\cdot\rangle$ is a time averaging operator.

147 The high frequency signal for mode-1 internal tides is written as

$$\widetilde{v} = \mathfrak{R}\left[\widetilde{v}_e(t)e^{i\omega t}\right] \text{ with } \mathfrak{R} \text{ the real part} \tag{3}$$

148 where $\widetilde{v}_e$ is the envelop of the oscillations of the tides and depends on the time, thus
149 capturing the non-stationarity of the waves. $\omega/2\pi$ is the frequency of the waves, 2 cycles
150 per day.

151 The internal tide signal can be decomposed into stationary and nonstationary contribu-
152 tions. The stationary part is defined with a coherent temporal averaging operator :

$$\widetilde{v}_s = \langle\widetilde{v}\rangle_c, \tag{4}$$

$$= \mathfrak{R}\left[\langle\widetilde{v}_e\rangle_c e^{i\omega t}\right] \tag{5}$$

153 Hence the nonstationary part, defined as the total velocity minus the stationary part :

$$\widetilde{v}_{ns} = \widetilde{v} - \langle\widetilde{v}\rangle, \tag{6}$$

$$= \mathfrak{R}\left[(\widetilde{v}_e - \langle\widetilde{v}_e\rangle_c)e^{i\omega t}\right] \tag{7}$$

154 Assuming the envelope of the nonstationary signal is exponential with a decay timescale
155 $\widetilde{T}$, the fast autocovariance is expressed as:

$$\widetilde{C}(\tau) = \left[\widetilde{V}_s^2 + \widetilde{V}_{ns}^2 e^{-\tau/\widetilde{T}}\right] \times cos(\omega\tau) \tag{8}$$

156 Following Veneziani et al. (2004) the turbulent velocity autocovariance is assumed to
157 have the form :

$$\overline{C}(\tau) = \overline{V}^2 e^{-\tau/\overline{T}} cos(\Omega\tau) \tag{9}$$

158 where $\overline{T}$ is the decorrelation timescale and Ω accounts for eddies and meanders.
159 The total autocovariance is then given by:

$$C(\tau) = \widetilde{C}(\tau) + \overline{C}(\tau) = \left[\widetilde{V}_s^2 + \widetilde{V}_{ns}^2 e^{-\tau/\widetilde{T}}\right] \times cos(\omega\tau) + \overline{V}^2 e^{-\tau/\overline{T}} cos(\Omega\tau) \tag{10}$$

160 This model is then fitted with the autocovariance obtained from our data and averaged
161 in bins in the y-direction. The variables $\widetilde{T}$, $\widetilde{V}_s$,$\widetilde{V}_{ns}$, $\overline{T}$, $\overline{V}$ and Ω are estimated to find the best

fit. The fit is done using a non linear least square regression (Jones et al. 2001–). Lower bounds are fixed to zero for all parameters except timescales, for which they are fixed at one day. The weight is uniform with no dependence on the timelag.

Because of drifters displacements across the domain, the time window used for the computation of Lagrangian autocovariances has to be short enough for the result to be typical of a specific area, while being long enough to capture the long decorrelation timescale. For each drifter's trajectory the velocity time series is split into segments of length T_w, overlapping each other by 50%. A time window of 40 day is chosen. Eulerian mean velocities, averaged in time and zonal direction is interpolated on drifters trajectories and removed. No significant impacts of this removal were observed on the results for the fast signal. The autocovariance is computed over each segment and averaged within 50 km wide meridional bins. Each segment is attributed to a bin depending on the mean position over the period T. We did not find a significant sensitivity of our results to the length of the window. The Eulerian autocovariance is computed at each grid point using the same time windows and bin-averaged meridionally as for the Lagrangian autocovariance. Autocovariances are then divided by the autocovariance at timelag zero to obtain the autocorrelation.

3. Signatures of internal tides and turbulent jet in Eulerian and Lagrangian perspective

a. Autocorrelation functions

Three main regimes stand out on Lagrangian and Eulerian 2D autocorrelation (function of timelag and y) (Fig.3 first and second column respectively), corresponding to typical drifters' trajectories shown in Fig2a, c and e. Autocorrelation at these latitudes of interest are further shown in Fig. 4. Fast oscillations, corresponding to the internal tides, are seen in the northern and southern parts of the domain for all autocorrelation functions. In these

areas, the signal seems to be dominated by internal tides, with a negligible influence of the slow advection of the drifters by the balanced flow. No decay of the amplitude of the oscillations with the time lag can be visually detected south of the domain, especially in the Eulerian perspective (see Fig. 4, panels e and f) indicating that internal tides are nearly stationary there. On the contrary, the amplitude of the fast oscillations decays mildly in the northern area, indicating internal tides non-stationarity. There are no significant visual differences between Lagrangian and Eulerian autocorrelations in the northern and southern areas. Conversely, the central area ($y \in [1000; 2000]$ km) exhibits a fast decay – especially in the Lagrangian perspective – of fast oscillations combined to a slower general decay associated with the slower jet turbulence. As observed in drifters trajectories and velocity time series (Fig. 2, panels c and d), Lagrangian diagnostics diverge from Eulerian ones in this area. The damping of fast oscillations in the central area occurs over a much shorter timescale in Lagrangian autocorrelation compared to Eulerian one : fast oscillations disappear after only a few days ($\tau \leq$5days) in Lagrangian perspective while they are still visible in the Eulerian one for the largest τ (20 days). The decorrelation of the slower motion is also faster in Lagrangian autocorrelation compared to Eulerian one, and exhibits a negative lobe around $\tau \sim 4$ days in the Lagrangian autocorrelation of v, which we attribute to the slow evolution of jet meanders. We also note that the autocorrelation of u does not decrease toward zero in the jet. Although this aspect is not the focus of our study, we attribute this to the fact that drifters oversample the meandering jet, resulting in a larger mean for the zonal velocity compared to the Eulerian mean. The fact that Eulerian autocorrelation decays more slowly than Lagrangian one is consistent with previous studies comparing Eulerian and Lagrangian decorrelation timescales (Lumpkin et al. 2002).

b. Estimates of velocity amplitudes and decorrelation timescales

To estimate Eulerian and Lagrangian decorrelation timescales and velocity amplitudes for both slow and fast motions, we fit the autocovariance from our data (Eulerian and Lagrangian) to the model given by eq. (10).

Eulerian and Lagrangian diagnostics (blue and red lines Fig. 5) show a loss of the stationarity of internal tides during the crossing of the jet. Eulerian stationary amplitude (Fig. 5c) exhibits high values relatively to the non-stationary one (Fig. 5d) ($\sim 0.06\,\mathrm{m\,s^{-1}}$ versus $\sim 0.01\,\mathrm{m\,s^{-1}}$) in the south with Eulerian envelope (Fig. 4 e and f) near constant indicating internal tides nearly stationary in this area. During the crossing of the jet, internal tides loss of stationarity is captured in Eulerian diagnostics as the nonstationary amplitude becomes larger than the stationary one, increasing up to $\sim 0.08\,\mathrm{m\,s^{-1}}$ in the northern part (y larger than $\sim 1700\,\mathrm{km}$), while the stationary part decreases slightly ($\sim 0.05\,\mathrm{m\,s^{-1}}$). A bump is observed in nonstationary amplitude due to the combined effects of a bump in stratification in the jet, Coriolis and the loss of stationarity. In this dominantly nonstationary area, nonstationarity timescales are between 10 and 20 days. We note that the Eulerian envelope in the north (blue lines Fig. 4a and b) does not seem to reach zero but a plateau, consistent with a remaining stationary component.

Lagrangian diagnostics present patterns significantly different from Eulerian ones as expected from drifters trajectories (Fig. 2 a, c and e) and autocorrelations (Fig. 3). In the south, the Lagrangian envelope (red lines Fig. 4 e and f) decays faster than Eulerian one. Lagrangian nonstationary and stationary amplitudes (red lines Fig. 5c and d) present similar values ($\sim 0.04\,\mathrm{m\,s^{-1}}$ for the stationary part and $\sim 0.03\,\mathrm{m\,s^{-1}}$ for the nonstationary part). Nonstationary timescales (Fig. 5a) remain between 10 and 20 days. In the jet area, the nonstationary amplitude largely dominates as it reaches values around $\sim 0.08\,\mathrm{m\,s^{-1}}$ while the stationary part decreases toward values smaller than $\sim 0.01\,\mathrm{m\,s^{-1}}$. Nonstationary timescale decreases rapidly in this region and reaches 1 day in its center. This apparent non-

stationarity in Lagrangian perspective is likely due to a dominant slow motion strongly advecting the drifters in this area. In the north, we observe a decay of Lagrangian autocorrelation envelope close to the Eulerian one. Stationary and nonstationary amplitude are similar to Eulerian ones with non-stationarity dominant. Timescales also have similar values, between 10 and 20 days. The non-stationarity in this area is captured similarly in both Lagrangian and Eulerian diagnostics.

The slow motion decorrelation timescales (Fig. 5b) reach their lowest values in the central area, ~20 day in Eulerian data and ~10 day in Lagrangian outputs. It corresponds to the area of high amplitude (Fig. 5e). It also coincides with the area of low Lagrangian non-stationarity timescales which supports an apparent non-stationarity in Lagrangian diagnostics dominant in this part. As seen in Lagrangian autocorrelation (Fig. 3), oscillations due to slow motion meanders are observed in the autocorrelation of v but well fitted by our model (Veneziani et al. 2004). The fit for the autocorrelation of u seems however to fail in the center of the jet with a decorrelation timescale of the slow motion overestimated in that bin as a tendency towards a value superior to zero is not expected by our model for slow motion.

c. Sensitivity to the jet's EKE

The sensitivity of internal tide nonstationarity timescales to the jet EKE is investigated with five numerical simulations of increasing jet's strength as shown by the meridional distributions of velocity amplitude (Figure 6b).

The jet strength, as measured by the velocity amplitude maximum value, varies by a factor of about 2 across five simulations (Fig.6b). The internal tides' total velocity amplitude, defined by $\sqrt{\widetilde{V}_s^2 + \widetilde{V}_{ns}^2}$, increases in the northern area with the jet's strength (Fig.6e). It increases with latitude similarly in both Eulerian and Lagrangian perspectives, regardless of the region of the domain or the jet's strength.

For the 2 most energetic simulations, S_3 and S_4, both Eulerian and Lagrangian diagnostics show a loss of stationarity of internal tides occurs when internal tides cross the jet. As in the previously studied simulation, the internal tides are nearly stationary in the southern area in Eulerian amplitudes (continuous lines in Fig. 6c and d) while Lagrangian stationary and nonstationary ones (circular markers in Fig. 6c and d) remain of similar order. In the jet, Eulerian and Lagrangian nonstationary amplitudes increase while Lagrangian stationary amplitude drops to zero. Lagrangian timescales (Fig. 6a) reach minimal values ($\leq$5days) while Eulerian ones remain around or above 10 days in every simulation. The width of this area increases with the jet's strength. As the drifters move along with the flow they might capture spatial variations as internal tides' non-stationarity . This may explain Lagrangian timescales shorter than Eulerian ones in the area where the slow motion dominates. In the northern area, the same pattern is found for the two cases : non-stationarity amplitudes and timescales are similar in both framework, the Lagrangian non-stationarity is not/weakly biased by the drifters' perspective. Interestingly, the intermediate case, S_2 exhibits features similar to $S-3$ and S_4 in the south and jet but distinct stationary amplitude and nonstationary timescale. The autocorrelation does not reach a plateau (stationary amplitude) in the chosen time window. This case is then considered

completely nonstationary in the north by our method, with small stationary amplitude and overestimated timescale. Contrary to previous cases, the two least energetic simulations, S_0 and S_1, show weak loss of stationarity in Eulerian perspective as the stationary amplitude remains dominant for all bins and the nonstationary timescales near the highest values allowed in our fitting procedure. Lagrangian stationary amplitude drops to zero in the jet as the nonstationary one exhibits a bump in the same area and the timescale drop to 1 day supporting Lagrangian apparent non-stationarity due to advection even for weakly energetic simulations.

4. Lagrangian model for autocovariance and comparison to fitted autocovariance

a. Theoretical expectation for the fast Lagrangian autocorrelation

We assume that the fast signal is a modulated monochromatic wave propagating in a single direction (say x) and characterized by a frequency ω and wavenumber k:

$$\tilde{v}(t) = \Re\left\{\widetilde{v}_e(x,t)e^{i(\omega t - kx)}\right\}, \tag{11}$$

where $\tilde{v}_e$ is the slowly varying envelope. Let's consider a parcel traveling with the flow with trajectory $X(t)$. The autocovariance of $\tilde{v}$ as measured along the parcel trajectory is given by:

$$\tilde{C}_L(\tau) = \langle \tilde{v}(t+\tau)\tilde{v}(t)\rangle, \tag{12}$$

$$= \frac{1}{2}\Re\left\{\left\langle \widetilde{v}_e\left[X(t+\tau),t+\tau\right]\widetilde{v}_e^*\left[X(t),t\right]e^{i\left[\omega\tau - k(X(t+\tau)-X(t))\right]}\right\rangle\right\}, \tag{13}$$

where we assume that fast oscillation terms ($\propto e^{\pm 2i\omega t}$) are smoothed out by the averaging procedure. Neglecting the contribution of the wave velocity to the displacement: $X(t) = \int^t \bar{v}(s)ds$, as well as the spatial dependency of the wave envelope (this point is discussed in the discussion, sect. b, below), and further assuming that the envelope of the wave and the slow flow are not correlated, we obtain:

$$\tilde{C}_L(\tau) = \Re\left\{\tilde{C}_E(\tau)\times\left\langle e^{i\left[\omega\tau - k(X(t+\tau)-X(t))\right]}\right\rangle\right\}, \tag{14}$$

where $\tilde{C}_E(\tau)$ is the autocovariance of the envelope. For the latter, we will re-use the model previously introduced in eq. (8), now denoting the Eulerian decorrelation term as $\tilde{T}_E$:

$$\tilde{C}_E(\tau) = \tilde{C}(\tau)/\cos(\omega\tau) = \tilde{V}_s^2 + \tilde{V}_{ns}^2 \exp(-\tau/\tilde{T}_E).$$

We assume now that the slow flow is a stationary Gaussian process, with a rms amplitude $\bar{V}$ (over one direction) and an exponential decorrelation in time with a typical time scale $\bar{T}$ – somewhat consistent with the model proposed in section 1, eq. (9) dropping the $\cos(\Omega\tau)$ term for simplicity. Such model – sometimes referred as an unbiased correlated velocity model in the literature (Gurarie et al.) – corresponds to the time-homogeneous Ornstein-Uhlenbeck process.

The displacement $\delta X = X(t+\tau) - X(t)$ is also a Gaussian process with null mean and variance given by (Pope 2015, Chap. 12):

$$\langle \delta X(t)^2 \rangle \equiv \sigma_X^2 = 2\bar{T}^2\bar{V}^2 \left[\tau/\bar{T} - \left(1 - e^{-\tau/\bar{T}}\right) \right]. \tag{15}$$

It is worth noting that the variance of the displacement admits two asymptotic regimes: $\sigma_X^2 \to \bar{V}^2\tau^2$ for $\tau \ll \bar{T}$, and $\sigma_x^2 \to 2\bar{V}^2\bar{T}\tau$ for $\tau \gg \bar{T}$. From this variance for the displacement, one obtains the final expression for the autocovariance of the fast motion in the Lagrangian frame:

$$\widetilde{C}_L(\tau) = \tilde{C}_E \int_{-\infty}^{\infty} \cos(\omega\tau - k\delta X) p(\delta X) d\delta X \tag{16}$$

$$= \left(\tilde{V}_s^2 + \tilde{V}_{ns}^2 \exp(-\tau/\tilde{T}_E)\right) \cos(\omega\tau) \int_{-\infty}^{\infty} \cos(k\delta X) \frac{e^{-\delta X^2/(2\sigma_X'^2)}}{\sigma_X' \sqrt{2\pi}} d\delta X \tag{17}$$

$$= \tilde{C} e^{-\sigma_X^2 k^2/2} = \tilde{C} \exp\left(-k^2\bar{V}^2\bar{T}^2 \left[\tau/\bar{T} - (1 - e^{-\tau/\bar{T}})\right]\right) \tag{18}$$

The resulting Lagrangian autocorrelation has no stationary part and decays faster than the Eulerian autocorrelation, as follows from the exponentially decay due to drifter transports. A non-dimensional parameter $k\bar{V}\bar{T}$ readily appears in this exponential, which compares the time taken by the a drifter to travel a wave length compare to the typical decorrelation

time of the slow flow. Several regimes are identified, depending on the effect of the advection, $k^2\sigma^2$, at a fixed time, typical of the decorrelation of the envelope :

- Weak advection ,$k^2\sigma^2 \ll 1$: The signature of the wave signal in the Lagrangian frame of reference matches the Eulerian one: $\widetilde{C_L}(\tau) \sim \widetilde{C_E}(\tau)$. Lagrangian stationary and non-stationary contributions directly reflect Eulerian ones. If $\widetilde{V}_{ns} \gg \widetilde{V}_s$, Eulerian is nonstationary. Amplitudes and non-stationarity timescales are expected to be similar in both perspectives. If $\widetilde{V}_{ns} \ll \widetilde{V}_s$, Eulerian signal is stationary.

- Strong advection, $k^2\sigma^2 \gg 1$: the Lagrangian perspective will deform the Eulerian one. $k\bar{V}\bar{T}$ will control the form of the Lagrangian envelope. If $k\bar{V}\bar{T} \gg 1$ the exponential decay of the Lagrangian autocorrelation scales is quadratic in τ with decay time scale $1/k\bar{V}$: $\widetilde{C_L}(\tau) \sim \tilde{V}_s^2 \cos(\omega\tau) \times e^{-k^2\bar{V}^2\tau^2}$. If $k\bar{V}\bar{T} \ll 1$ the slow flow decorrelation induces a linear exponential decay with decay time scale $1/k^2\bar{V}^2\bar{T}$: $\tilde{V}_s^2 \cos(\omega\tau) \times e^{-k^2\bar{V}^2\bar{T}\tau}$

This predicted form of the autocorrelation in the Lagrangian framework is in qualitative agreement with the Lagrangian autocorrelations shown on Fig. 5 and 6. In particular, the stationary part of the fitted Lagrangian autocorrelation becomes negligible in a large region around the jet latitude. The fact that it is not zero at the very south and very north of the domain is due to the fact that the parameter $k\bar{V}\bar{T}$ is very small in this region, associated with a very slow decay of the Lagrangian envelop (see also Fig. 3), which implies a non-vanishing stationary fraction as recovered by the model fit from eq. (8).

b. Comparison of fitted autocovariances to predicted Lagrangian ones

The predicted Lagrangian autocovariance's envelope (Fig. 7 right column) is computed from the fitted Eulerian autocovariance envelope (Fig. 7 left column) following Eq. (18) so that it may be compared to the fitted Lagrangian one (Fig. 7 middle column). For all simulations (S_0, S_2 and S_4 shown in Fig. 7, first, second and third line respectively),

the Eulerian autocorrelation envelope's decay rate increases from south to north and with the jet's strength as commented previously. This is expected of a loss of stationarity as the wave propagates northward. For the fitted Lagrangian autocorrelation however, low values of the envelop are reached for small time lags in the jet due to the advection in the area. In the northern part the Lagrangian envelope exhibits slower decay rates that tend to Eulerian ones. The predicted Lagrangian autocorrelation envelope reaches values inferior to 0.1 for time lags smaller than 5 days in the center of the domain which is consistent with what is observed in the fitted Lagrangian autocorrelation in a strong advection area. In northern and southern area, the advection impact represented in the predicted autocorrelation also fits what is observed in fitted Lagrangian autocorrelation with decay rates qualitatively close to the Eulerian ones. This decay seems however slightly overestimated (values smaller than 0.2 for τ>30 days when similar values are not reached in Eulerian or Lagrangian fits). Overall, following Eq. (18), the differences between Lagrangian and Eulerian can be qualitatively explained as the effect of drifters being advected by the slow motion.

Depending on the significance of Eulerian non-stationarity and the relative importance of $\widetilde{T}_L/\widetilde{T}_E$ and $k^2\sigma^2(\widetilde{T}_L)$ (Fig. 8b and c, respectively), the Lagrangian non-stationarity timescale is likely due to Eulerian non-stationarity or drifters strong advection by slow motion. For simplification sake, both terms will be referred to as $r_E(\widetilde{T}_L)$ and $r_{adv}(\widetilde{T}_L)$ respectively.

In the southern area, the ratio of Eulerian nonstationary and stationary amplitudes (Fig. 8a) is smaller than one for all simulations, internal tides area stationary. The advection is weak, $r_{adv}(\widetilde{T}_L) \ll 1$. The Eulerian nonstationary timescale has no significant impact on the form of envelope in this area and its estimation is expected not to be significant. r_E is found larger than one is this area, however a Lagrangian timescale larger than Eulerian one cannot be explained by our model. As stipulated previously, this can be due to

an underestimation of the Eulerian timescale. It also could be caused by an estimation error of Lagrangian nonstationary timescale and/or the result of an inappropriate form of decay employed for the fit (e.g. linear exponential decay vs quadratic) for Lagrangian autocovariance as the slow motion decorrelation timescale is of the order of the time window size (40 days).

Northern and central areas illustrate the two different regimes for internal tides non-stationarity in Lagrangian data, described in the previous subsection. In the north, ratio of nonstationary and stationary amplitudes is larger than one for S_2, S_3 and S_4, where nonstationary amplitudes dominates. For least energetic slow motion (S_0 and S_1) stationary tide still dominates but with significant nonstationary contribution. The advection term, r_{adv} is small in the north and r_E values are around 1 : the Lagrangian autocovariance is close to the Eulerian one, following eq.(18). The non-stationarity captured in Lagrangian perspective corresponds to the one in Eulerian perspective. In the jet, the ratio of Eulerian nonstationary and stationary amplitudes increases with nonstationary component not yet dominant. In the same area, r_E is small as the Lagrangian timescale is small in front of the Eulerian one, the decorrelation is faster in Lagrangian perspective than in Eulerian one. This coincides with r_{adv} around 1, the internal tides' non-stationarity captured in the Lagrangian perspective is due to advection by slow motion. We call this non-stationarity, apparent non-stationarity.

5. Discussion

a. Lagrangian apparent non-stationarity

We now discuss the reported alteration of the internal tide surface signature in the Lagrangian perspective in the more general context of observation of ocean high-frequency dynamics. Low mode internal tides have by definition large vertical scales – similar to that of the background flow. Advection by the slow flow is of particular importance for

discussing the Eulerian/Lagrangian distorsion, even though it does not fully capture the interaction between the slow flow and the internal tide (Dunphy et al. 2017; Savage et al. 2020). A vertical mode expansion of equations of motions linearized around the slow background flow shows that advection of the internal tide mode is driven by a non-trivial weighted average of the background flow.

This effective advection is expressed as $H^{-1}\int_{-H}^{0}\phi_n^2\mathbf{U}dz$ (Kelly and Lermusiaux 2016), where ϕ_n is the standard pressure mode for an internal wave with vertical mode number n (see also Duda et al., for a more technical approach).

Thus, for a surface intensified background flow, the flow advecting the drifter (at the surface) and the one advecting the internal tide mode is different, explaining why the Lagrangian observer renders a distorted view of the internal wave signal.

For the simulation with moderate jet intensity S2, for instance, the mode 1 effective advection velocity (computed, but not shown) is of order $0.2\,\mathrm{m\,s^{-1}}$ at its maximum, while the surface velocity is typically greater than $1\,\mathrm{m\,s^{-1}}$: the Eulerian distortion, driven by the effective advection velocity, is therefore smaller than the Lagrangian distortion, driven by the difference between this effective advection and the surface velocity transporting the drifter.

This somewhat justifies a central approximation of the theoretical model derived in section a, where we neglected the advection of the wave by the slow flow.

For small scale internal waves on the other hand, ray theory can be used to describe their propagation through the background flow (Broutman et al. 2004). This approach shows that wave packets are advected by the local flow, which is associated with a Doppler shifting of the Eulerian frequency: $\omega = \hat{\omega} + \mathbf{k}\cdot\mathbf{U}$, where ω and $\hat{\omega}$ are respectively the wave absolute (or Eulerian) and intrinsic (as measured in a frame of reference moving with the slow flow) frequencies, $\mathbf{k}$ is the wave vector, and $\mathbf{U}$ is the slow flow.

Ignoring advection of the drifter by the wave current, the signal measured by the drifter coincides with the wave field in the frame comoving with the mean flow with least distortion in the Lagrangian frame of reference.

This situation is opposite to the configuration investigated here, as Lagrangian auto-correlation exhibits faster decrease with time lag compared to Eulerian auto-correlation, and the theoretical model proposed here would obviously not be relevant.

In a realistic configuration, the range of validity of each of these two regimes (e.g. small vs large scale waves) remains to be quantified.

b. On internal tide non-stationary spatial envelope

Another assumption of the theoretical model is that the spatial envelope of the wave is spatially uniform but temporally variable. In reality the envelope of the wave propagates with the internal tide group speed resulting in spatial variability if a temporal one is admitted. We assume the typical size of the envelope should however scale as the product of the group velocity and the Eulerian non-stationary time scale and that this will in general be larger than several wavelengths. The apparent non-stationarity relies on the conversion of the spatial variability at the scale of a wavelength and thus do not expect the spatial variability of the envelope would affect the form (10) at first order. Synthetic experiments could help verify this point. If necessary, the spatial inhomogeneities of the wave envelop could be included in the model, at the cost of adding complexity. This, however, requires additional to characterize these spatial inhomogeneities (through spatio-temporal autocovariance), which has not been reported in the context of internal tides – to our knowledge.

c. Autocorrelations models and sationary/non-stationary decomposition

Several ad-hoc choices have been made regarding the shape of internal tide and slow motion autocorrelation. Limits to these choices are visible on Figure 4c for slow motions

and are speculated to affect estimates of internal tide nonstationary time scales in the southern part of the domain. The internal tide envelope autocorrelation initially chosen included a single exponential decaying term instead of the sum of stationary/nonstationary contributions. We abandoned eventually this choice as it does not naturally lead to the decomposition of the signal into stationary/non-stationary contributions as well as was required to consider time scales overly large in stationary cases (>1000 days). One may also have fitted the more general form (Eq.(18)) to Lagrangian autocorrelations, for example, and evaluated its relevance compared to the single linear term exponential form. This would add one more parameter to estimate however and would require to determine whether this more general form leads to an improvement which we felt was a study on its own. We did not attempt to do this eventually in favor of a more qualitative assessment of the theory. Determining what form is more appropriate to describe the Eulerian and Lagrangian internal envelope autocorrelation is a study on its own that would best reserved to realistic configurations.

6. Conclusion

In order to investigate the use of Lagrangian data to characterize internal tides propagating through a turbulent jet, we compare Eulerian and Lagrangian internal tides characteristics in an idealized simulation. Characteristics of mode-1 internal tides were estimated via fitting data in both perspectives and an internal tide autocovariance envelope including the sum of a constant stationary contribution and an exponentially decaying nonstationary one.

Near their generation site and far from the jet, internal tides are found to be nearly stationary in Eulerian perspective. As internal tides propagate through the jet (i.e. energetic area), the drifters are strongly advected by slow motions which causes Lagrangian non-stationary timescales to be lower than Eulerian ones. We call this

phenomenon, found in Lagrangian perspective, apparent non-stationarity. After crossing the jet, internal tides propagate in an area of weaker energy but have lost stationarity. Internal tides non-stationary amplitude is significant there and even dominates in the most energetic cases. In this area, the intrinsic non-stationarity captured in Eulerian diagnostics is present similarly in Lagrangian amplitudes and timescales. Regardless of slow motion amplitude or Eulerian stationarity of internal tides the total amplitude (stationary and nonstationary components) is successfully recovered in Lagrangian perspective. The deformation of internal tides characteristics in Lagrangian perspective was qualitatively predicted by a theoretical model for Lagrangian autocovariances (eq.(18)). This model modifies Eulerian autocovariances to take into account the advection of drifters.

One of the main result of this study is the estimation of the total amplitude in Eulerian and Lagrangian perspectives using autocovariances and parametric fit instead of non-parametric spectral analysis. This method has the advantage to avoid the dependence on an arbitrary choice of frequency band. Indeed, in spectral analysis the chosen band has a strong impact on evaluating the energy contribution of motions identified by their frequency (Yu et al. 2019). This choice is further complicated by the variation of the width of tidal peaks depending on the internal tides' stationarity and drifters advection by slow motion, in the case of Lagrangian spectra. Parametric spectral analysis could be explored as an alternative to free from this constraint. The efficiency of our method should also be investigated in a more realistic set-up.

Lagrangian diagnostics and their comparison to Eulerian ones should help to assess how drifters data could be used, notably in the context of SWOT. As Lagrangian and Eulerian total amplitudes were found to be similar, Lagrangian estimates could help to identify where the internal tides contribution to ocean surface energy would be significant. This leading to where balanced flow and internal tides could be entangled in SWOT

data. It involves however a transition from internal tides kinetic energy amplitude to pressure, which should be investigated. In areas of weak advection, we might be able to separate stationary and non-stationary amplitudes in Lagrangian data. The theoretical model developed in this study should help to define regimes for which this separation is possible. Areas of high non-stationary internal tides contribution and therefore of difficult prediction of internal tides may thus be flagged. Note that these specific regions are also the ones where we found a correct estimation of non-stationarity timescales. Again these preliminary results should be investigated in a realistic set-up, numerical model or in situ data.

This potential information brought by Lagrangian data could also be complementary material to map internal tides. Mappings of internal tides have been studied from altimetry (Zaron 2017, 2019). Drifters data, via an estimation of total amplitude, might contribute to this mapping, setting at least an upper limit to stationary and nonstationary amplitudes. A direct decomposition of total amplitude in stationary and nonstationary components may also be derived, in some cases, from drifters data, as noted previously.

As anticipated in other studies (Zaron and Elipot 2020), apparent non-stationarity was found in our Lagrangian data and predicted by our theoretical model, in areas of strong advection. Areas and regimes for which Lagrangian perspective would deform internal tides characteristics may be flagged. It could have consequences on the use of Lagrangian filtering to filter out tidal signal from surface data. Indeed, low decorrelation timescales translate in the frequency domain by a broadening of tidal peaks which is expected to complicate the separation of motions by their frequency.

The estimation of internal tides contribution in ocean surface energy through the total – and, in some cases, of stationary and nonstationary – amplitudes from drifters data might also help to validate realistic models resolving high frequency variability.

In the shorter term, a natural extension of our study is to apply our findings to the analysis of actual drifter trajectories or numerically predicted ones in realistic simulations. Eulerian outputs from a realistic simulation (LLC4320) have already been compared to drifters data (Yu et al. 2019). A future study will aim at applying our findings to simulated drifter trajectories from the same numerical simulation. Similar methods applied to energetic regions of the globe would allow us to test our method and analytical models to more realistic set-ups in particular to compare Lagrangian and Eulerian amplitudes and non-stationarity timescales.

References

Broutman, D., J. W. Rottman, and S. D. Eckermann, 2004: Ray Methods for Internal Waves in the Atmosphere and Ocean. **36 (1)**, 233–253, doi:10.1146/annurev.fluid.36.050802.122022.

Buijsman, M. C., B. K. Arbic, J. G. Richman, J. F. Shriver, A. J. Wallcraft, and L. Zamudio, 2017: Semidiurnal internal tide incoherence in the equatorial p acific. *Journal of Geophysical Research: Oceans*, **122 (7)**, 5286–5305.

Davis, R., 1983: Oceanic property transport, lagrangian particle statistics, and their prediction. *Journal of Marine Research*, **41 (1)**, 163–194.

Davis, R. E., 1985: Drifter observations of coastal surface currents during CODE: The method and descriptive view. *J. Geophys. Res.*, **90(C3)**, 4741–4755.

Duda, T. F., Y.-T. Lin, M. Buijsman, and A. E. Newhall, ????: Internal Tidal Modal Ray Refraction and Energy Ducting in Baroclinic Gulf Stream Currents. **48 (9)**, 1969–1993, doi:10.1175/JPO-D-18-0031.1.

Dunphy, M., A. L. Ponte, P. Klein, and S. Le Gentil, 2017: Low-mode internal tide propagation in a turbulent eddy field. *Journal of Physical Oceanography*, **47 (3)**, 649–665.

Elipot, S., R. Lumpkin, R. C. Perez, J. M. Lilly, J. J. Early, and A. M. Sykulski, 2016: A global surface drifter data set at hourly resolution. *Journal of Geophysical Research: Oceans*, **121 (5)**, 2937–2966.

Elipot, S., R. Lumpkin, and G. Prieto, 2010: Modification of inertial oscillations by the mesoscale eddy field. *Journal of Geophysical Research: Oceans*, **115 (C9)**.

Fu, L.-L., D. Alsdorf, R. Morrow, E. Rodriguez, and N. Mognard, 2012: Swot: The surface water and ocean topography mission: Wide-swath altimetric elevation on earth. Tech. rep., Pasadena, CA: Jet Propulsion Laboratory, National Aeronautics and Space . . . .

Garrett, C., and E. Kunze, 2007: Internal tide generation in the deep ocean. *Annu. Rev. Fluid Mech.*, **39**, 57–87.

Gurarie, E., C. H. Fleming, W. F. Fagan, K. L. Laidre, J. Hernández-Pliego, and O. Ovaskainen, ????: Correlated velocity models as a fundamental unit of animal movement: Synthesis and applications. **5 (1)**, 13, doi:10.1186/s40462-017-0103-3.

Jones, E., T. Oliphant, P. Peterson, and Coauthors, 2001–: SciPy: Open source scientific tools for Python: Least square regression. [Available online at https://docs.scipy.org/doc/scipy/reference/generated/scipy.optimize.curve_fit.html].

Kelly, S. M., and P. F. J. Lermusiaux, 2016: Internal-tide interactions with the Gulf Stream and Middle Atlantic Bight shelfbreak front. **121 (8)**, 6271–6294, doi:10.1002/2016JC011639.

LaCasce, J., 2008: Statistics from lagrangian observations. *Progress in Oceanography*, **77 (1)**, 1–29.

562 Lumpkin, R., A.-M. Treguier, and K. Speer, 2002: Lagrangian eddy scales in the northern
563 atlantic ocean. *Journal of physical oceanography*, **32 (9)**, 2425–2440.

564 Middleton, J. F., 1985: Drifter spectra and diffusivities. *Journal of Marine Research*,
565 **43 (1)**, 37–55.

566 Morrow, R., and Coauthors, 2019: Global observations of fine-scale ocean surface topog-
567 raphy with the surface water and ocean topography (swot) mission. *Frontiers in Marine*
568 *Science*, **6**, 232.

569 Nash, J. D., S. M. Kelly, E. L. Shroyer, J. N. Moum, and T. F. Duda, 2012a: The unpre-
570 dictable nature of internal tides on continental shelves. *Journal of Physical Oceanog-*
571 *raphy*, **42 (11)**, 1981–2000.

572 Nash, J. D., E. L. Shroyer, S. M. Kelly, M. E. Inall, T. F. Duda, M. D. Levine, N. L. Jones,
573 and R. C. Musgrave, 2012b: Are any coastal internal tides predictable? *Oceanography*,
574 **25 (2)**, 80–95.

575 Nelson, A. D., B. K. Arbic, E. D. Zaron, A. C. Savage, J. G. Richman, M. C. Buijsman, and
576 J. F. Shriver, 2019: Toward realistic nonstationarity of semidiurnal baroclinic tides in a
577 hydrodynamic model. *Journal of Geophysical Research: Oceans*, **124 (9)**, 6632–6642.

578 Ponte, A. L., and P. Klein, 2015: Incoherent signature of internal tides on sea level in
579 idealized numerical simulations. *Geophysical Research Letters*, **42 (5)**, 1520–1526.

580 Ponte, A. L., P. Klein, M. Dunphy, and S. Le Gentil, 2017: Low-mode internal tides and
581 balanced dynamics disentanglement in altimetric observations: Synergy with surface
582 density observations. *Journal of Geophysical Research: Oceans*, **122 (3)**, 2143–2155.

583 Pope, S. B., 2015: *Turbulent Flows*. Cambridge Univ. Press, 771 pp.

584 Ray, R. D., and E. D. Zaron, 2016: M2 internal tides and their observed wavenumber
585 spectra from satellite altimetry. *Journal of Physical Oceanography*, **46 (1)**, 3–22.

Savage, A., and Coauthors, 2020: Low-mode internal tides and small scale surface dynamics in the swot cal/val region. *Ocean Sciences Meeting 2020*, AGU.

Savva, M. A., and J. Vanneste, 2018: Scattering of internal tides by barotropic quasi-geostrophic flows. *Journal of Fluid Mechanics*, **856**, 504–530.

Veneziani, M., A. Griffa, A. M. Reynolds, and A. J. Mariano, 2004: Oceanic turbulence and stochastic models from subsurface lagrangian data for the northwest atlantic ocean. *Journal of physical oceanography*, **34 (8)**, 1884–1906.

Whalen, C. B., C. de Lavergne, A. C. N. Garabato, J. M. Klymak, J. A. Mackinnon, and K. L. Sheen, 2020: Internal wave-driven mixing: governing processes and consequences for climate. *Nature Reviews Earth & Environment*, **1 (11)**, 606–621.

Yu, X., A. L. Ponte, S. Elipot, D. Menemenlis, E. Zaron, and R. Abernathey, 2019: Surface kinetic energy distributions in the global oceans from a high-resolution numerical model and surface drifter observations. *Geophys. Res. Lett.*

Zaron, E. D., 2017: Mapping the nonstationary internal tide with satellite altimetry. *Journal of Geophysical Research: Oceans*, **122 (1)**, 539–554.

Zaron, E. D., 2019: Baroclinic tidal sea level from exact-repeat mission altimetry. *Journal of Physical Oceanography*, **49 (1)**, 193–210.

Zaron, E. D., and S. Elipot, 2020: An assessment of global ocean barotropic tide models using geodetic mission altimetry and surface drifters. *Journal of Physical Oceanography*.

List of Figures

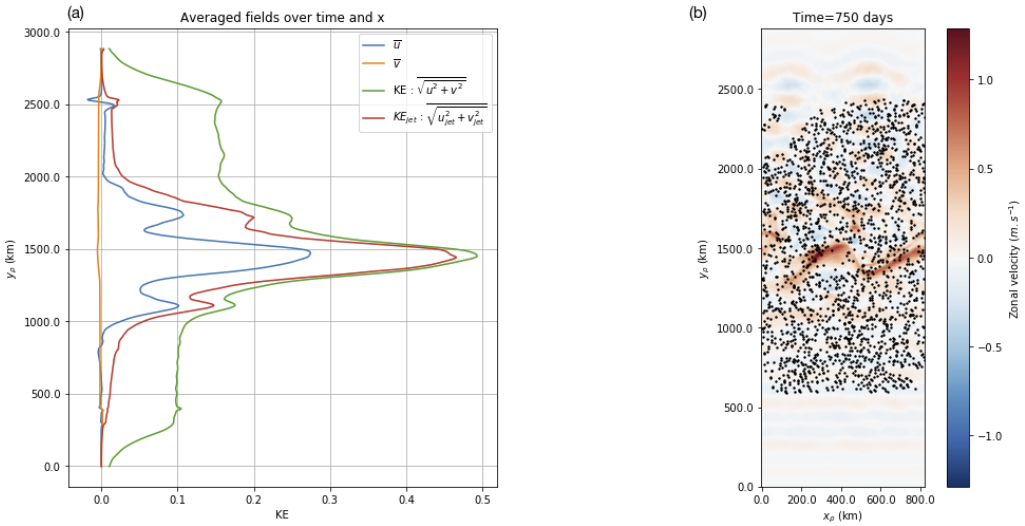

Figure 1. (a) : Mean field of zonal (blue line), meridional (orange line), total (green) and low-passed (red) velocity amplitudes ; (b) : Zonal velocity at t=750 days (color) with positions of 1/4 of the drifters at the same time represented by black dots.

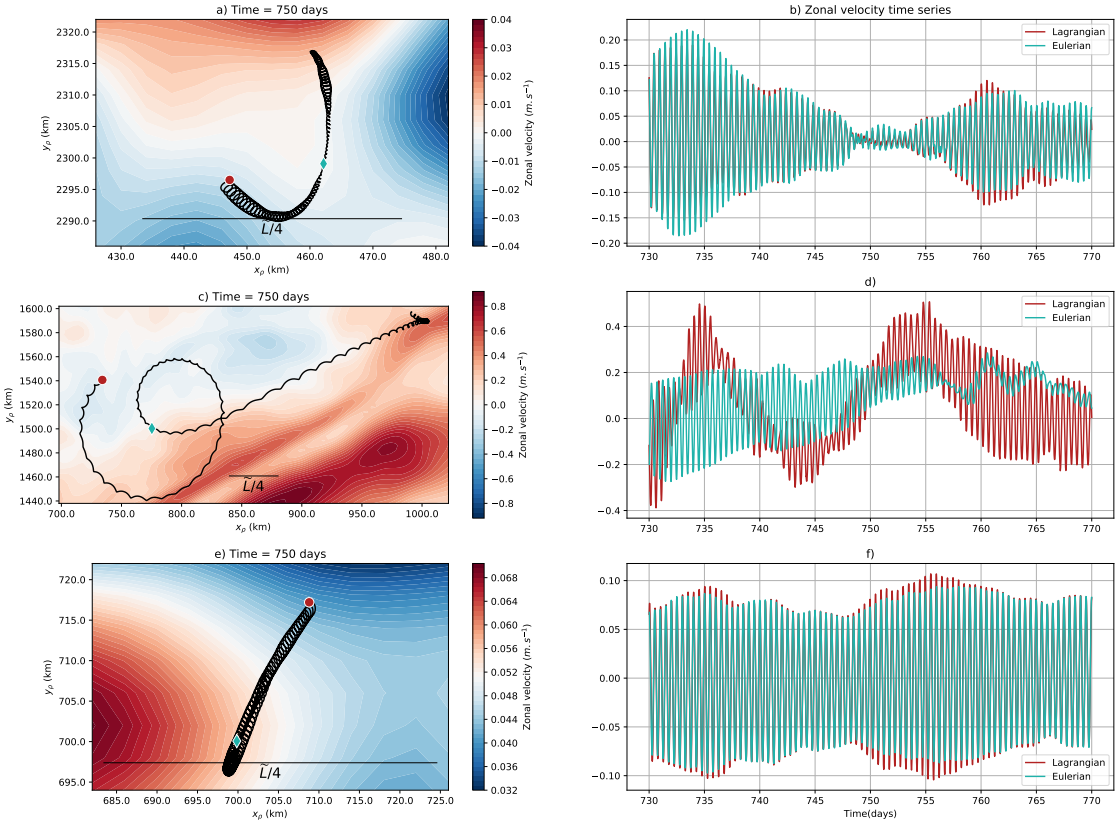

649 Figure 2. Trajectories of 3 drifters in three different area of the domain (north (a and b), central
650 (c and d) and south (e and f)) over a period of 40 days and corresponding time series. Left column
651 : Trajectory of each the drifter (black line) with the zonal velocity in the background. The red circle
652 represents the position of the drifter at t0 and the blue diamond the position at mid period. A black
653 straight line is plotted representing a quarter of the wavelength. Right column : Zonal velocity time
654 series along the drifter trajectory in red and at a fixed position (blue diamond in the left figure) in blue.

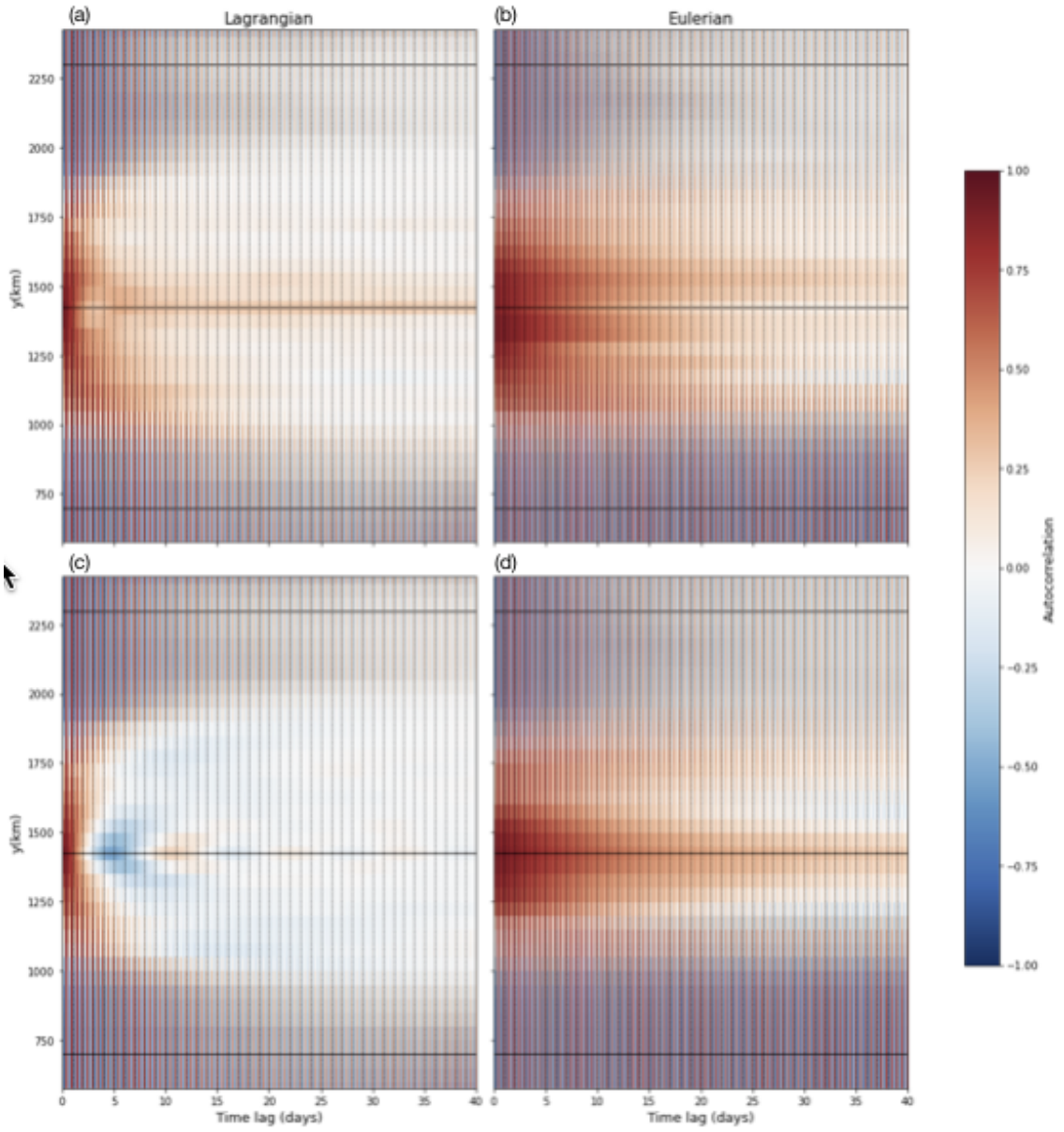

Figure 3. Autocorrelation of u (a and b) and v (c and d) computed from Lagrangian outputs (a and c) and Eulerian one (right column : b and d). The y-axis corresponds to the y bins in which the autocorrelation have been averaged. In the x-axis is the time lag. Horizontal black lines indicate the three latitudes of interest discussed in the paper (see Figs. 2 and 4)

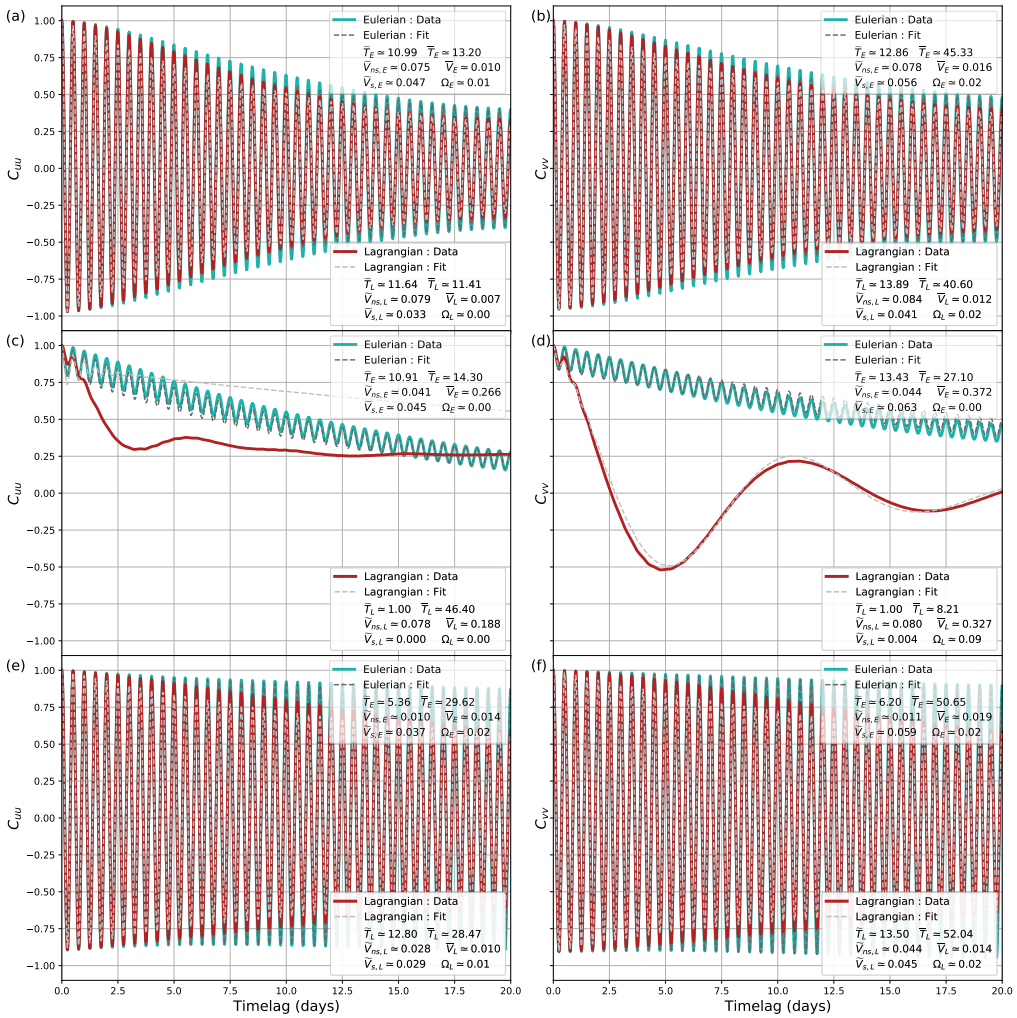

Figure 4. Autocorrelation at fixed bin in three different area : north (a and b), center (c and d) and south (e and f) of the domain). The Eulerian and Lagrangian autocorrelation derived from our data are represented respectively in blue and red. The autocorrelation corresponding to the best fit of our theoretical model with the autocovariance are plotted in grey dashed lines. Corresponding values of the fitted parameters are indicated in each panel.

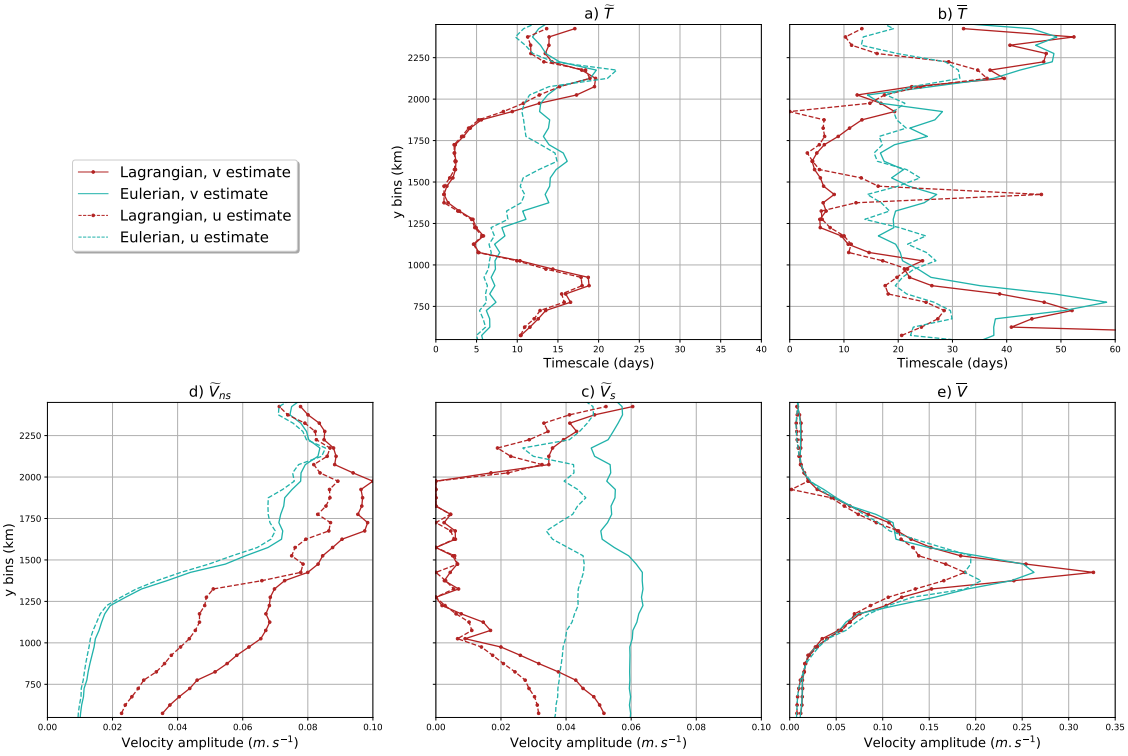

Figure 5. Estimated eulerian (blue lines) and Lagrangian (red lines with circular markers) non-stationarity, $\widetilde{T}$ (a) and decorrelation of the balanced flow, $\overline{T}$ (b) timescales and fast and slow components amplitudes, $\widetilde{V}_{ns}$ (c), $\widetilde{V}_s$ (d) and $\overline{V}$ (e). The estimates are found by fitting the theoretical model (Eq.(18)) to the autocorrelation of u (dashed lines) and v (continuous lines).

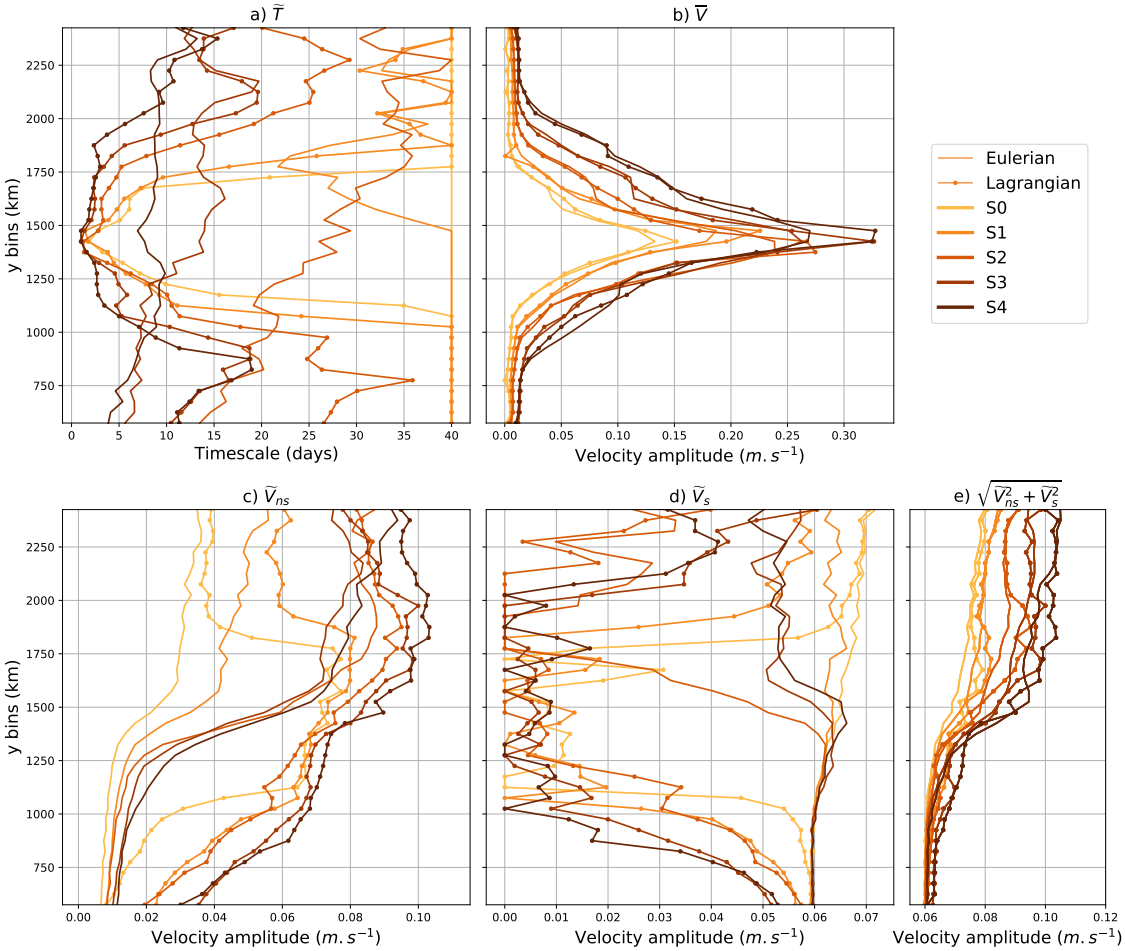

Figure 6. Estimated parameters for five simulations. (a) Lagrangian and Eulerian internal tides nonstationary timescales, $\widetilde{T}$. (c), (d) and (e) : Fast components nonstationary and stationary velocity amplitudes, $\widetilde{V}_{ns}$ and $\widetilde{V}_s$ and total amplitude, $\sqrt{\widetilde{V}_{ns}^2 + \widetilde{V}_s^2}$. Slow component velocity amplitude, $\overline{V}$ (b) is also represented. Timescales lower than 1 day and larger than 40 days were not allowed by our fitting procedure.

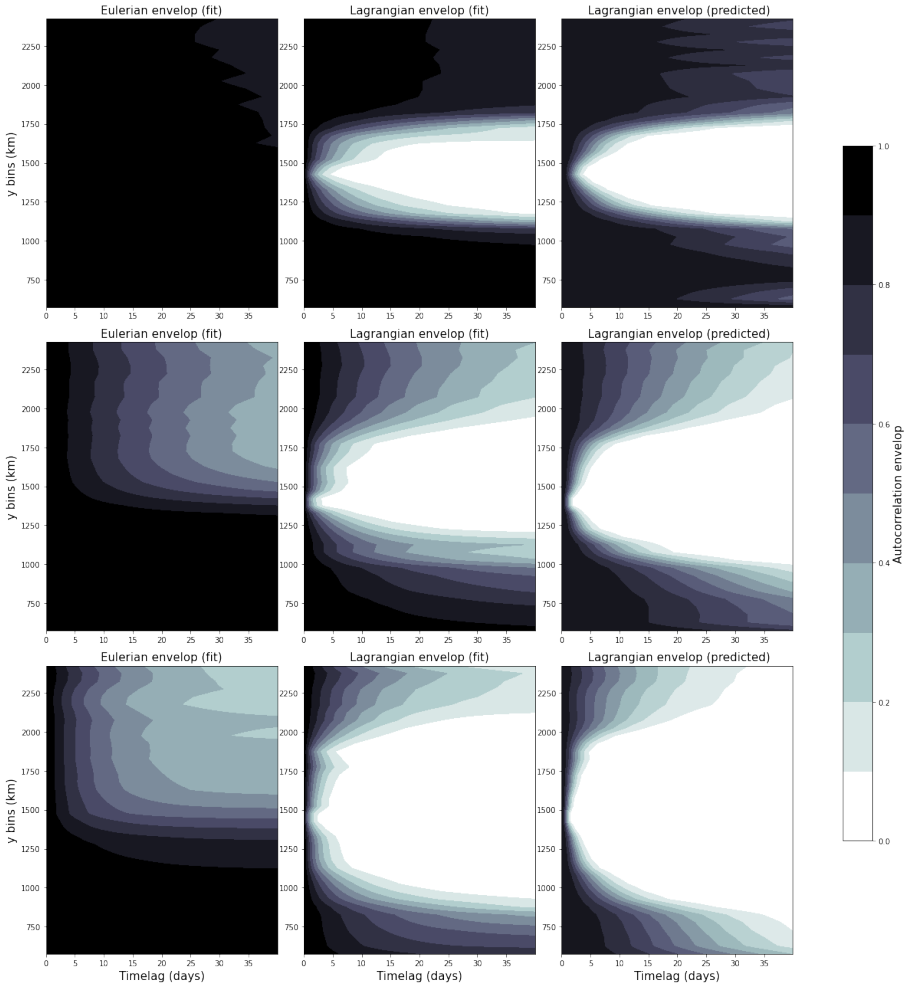

673 Figure 7. Amplitude of the envelop of fast oscillation in autocorrelation functions for 3 simulations
674 (corresponding to rows). From top to bottom the jet's strength increases. The envelope of the
675 fitted Eulerian (left column) and Lagrangian (middle column) autocorrelation as well as the predicted
676 Lagrangian autocorrelation (right column) are plotted.

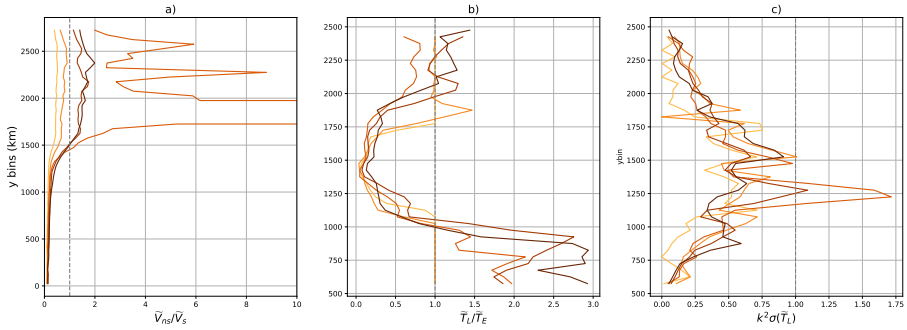

677 Figure 8. Ratio $\widetilde{V}_{ns}/\widetilde{V}_s$ (a) and $\widetilde{T}_L/\widetilde{T}_E$ (b) as well as the term in the exponential (Eq. (18)), $k^2\sigma(\widetilde{T}_L)$,
678 (c) are represented.